Magneto-transport behavior of disordered three dimensional Ni_xCo_{1-x} inverse opal networks

H. E. Torres Soto

Instituto de Investigaciones en Materiales - Unidad Morelia, Universidad Nacional Autónoma de México.
Antigua Carretera a Pátzcuaro No. 8701 Col. Ex Hacienda de San José de la Huerta, 58190, Morelia, Mexico.

F. Abreu Araujo

Institute of Condensed Matter and Nanosciences, Université Catholique de Louvain,
Place Croix du Sud 1, 1348 Louvain-la-Neuve, Belgium.

J. de la Torre Medina

Instituto de Investigaciones en Materiales-Unidad Morelia, Universidad Nacional Autónoma de México,
Antigua Carretera a Pátzcuaro No. 8701 Col. Ex Hacienda de San José de la Huerta, 58190, Morelia, México.

Herein we report on the magneto-transport properties of disordered three dimensional inverse opals (3D-IOs) fabricated by a standard three-probe electrodeposition technique into the interstices of porous membranes made of 150 nm diameter self assembled poly(methyl methacrylate) spheres. This approach has allowed the synthesis of large scale nanocomposites with exact ferromagnetic Ni_xCo_{1-x} alloy compositions and complex interconnected structure. Particularly, the microstructure of Co-rich 3D-IOs is consistent with the hexagonal close packed *hcp* texture and its corresponding magnetoresistance is explained in terms of the *hcp* Co magnetocrystalline anisotropy contribution. Conversely, the magnetoresistive behavior of Ni-rich 3D-IO networks is explained in terms of only their magnetostatic field. The control of these features is made possible by the reduced dimensions of necks and walls, in the 40 nm to 60 nm range, of the 3D-IO structure. Despite the disordered morphology of these 3D-IO nanoarchitectures, their microstructural and magneto-transport properties can be fine tuned due to the reduced nanoscale dimensions of the electrical interconnections. These properties have been found to be comparable to those obtained in other 3D networks, making them interesting systems for their potential use for magnetic sensing and spintronic applications.

1. Introduction

Magnetic arrays of interconnected nanostructures are appealing systems due to their interesting properties and potential applications as high density magnetic storage media, magnetic sensing and spintronic device applications [1, 2]. Two dimensional (2D) ordered antidot arrays obtained by patterning of magnetic thin films using techniques like electron beam lithography and nanosphere lithography, are among the most studied large scale interconnected magnetic systems [3, 4]. Although 2D systems are very interesting for the study of different phenomena like magnetic frustration, emergent magnetic monopoles and magnonics [5], they are limited to the study of effects characteristic of three dimensional (3D) nanomagnetism [6] and are not suitable for non-planar applications [7]. The development of more complex nano-architectures allowing interconnections in three dimensions between basic nano-building blocks have attracted further attention due to the possibility of fabricating large scale macroscopic systems with unique functionalities based on nanoscale properties. That is, 3D materials build from basic nanoelements with specific morphological and physico-chemical properties have attracted considerable interest for a large variety of potential applications [8–13]. Control on

the spatial and microstructural characteristics has lead to the development of different types of 3D magnetic nanoarchitectures like crossed nanowire networks [14, 15], interconnected carbon based nanofibers [16], and inverse opals [17]. Three dimensional inverse opals (3D-IOs) networks grown into the interstices of self-assembled polymeric spherical particles have attracted considerable attention due to their use as electrochemical energy storage [18–20], catalysts [21], thermoelectrics [22], photoanodes for solar water oxidation [23], photonic [24], and biological and chemical sensing [25] devices. Among the wide variety of fabrication methods to synthesize nanostructured networks, electrodeposition has been widely particularly used as a tool for the growth of 3D-IOs into the interstices of self assembled colloidal crystals made of ensembles of polymeric nanoparticles [26–29]. Electrodeposition, as a versatile and low cost fabrication technique, allows the synthesis of complex 3D networks for a wide variety of applications. Specifically, magnetic 3D-IOs fabricated as large scale nanoarchitectures have been found to exhibit interesting microwave absorption [30], magnetic [31], spin wave modes [32] and magneto-transport [33] properties for their potential use as multifunctional devices. Among these, magneto-transport properties like anisotropic magnetoresistance (AMR) and giant magnetoresistance are well-known ef-

fects that have been exploited for a wide variety of spintronic applications [34]. Particularly, 3D-IOs displaying AMR signals [35] are potential candidates for large scale spintronic applications.

In this work a series of Ni_xCo_{1-x} 3D-IOs, with $0 \leq x \leq 1$, have been synthesized by electrodeposition into the interstitial voids of polymeric opals made of self assembled spherical Poly (methyl methacrylate) (PMMA) nanoparticles. The microstructural and magnetic characterization has shown that Co-rich 3D-IOs have *hcp* texture and their corresponding magnetocrystalline anisotropy leads to significant changes in the magnetoresistance curves. Conversely, Ni-rich 3D-IOs have preferential *fcc* texture and display more symmetrical magnetoresistance curves with larger AMR values. Despite the disorder feature of the 3D-IOs synthesized in this work, their magnetic and magneto-transport behavior is very comparable and of the same order of magnitude as that of other 3D networks [36–38], which makes them interesting for magnetic sensing and spintronic applications.

2. Experimental

Previously cleaned microscope slides using FL-70 phosphate-free soap and nitric acid have been used as substrates for conductive indium-tin oxide (ITO) thin films that serve as cathodes for the growth of inverse opals. The ITO thin films have been spin-coated on the as-cleaned microscope slides by following a previously reported citric acid sol-gel route [39]. A solution has been prepared by dissolving 1.1 mmol $C_6H_8O_7 \cdot H_2O$ + 0.5 mmol $InCl_3 \cdot 4H_2O$ + 0.05 mmol $SnCl_4 \cdot 5H_2O$ in a mixture of 3 mL ethanol and 2 mL ethylene glycol at 40 °C for 30 min. All reactants are 99.9% pure and were purchased from Aldrich. For the spin-coating process, a 40 μL solution volume is dropped onto the substrate which is accelerated at 5000 rpm for 10 s. The as-obtained ITO thin layer is dried on a hot plate at 100°C and then sintered in a furnace in ambient conditions at 500°C for one hour. PMMA nanoparticles have been synthesized by a controlled pH emulsion polymerization [40]. In this process, the monomer is dispersed in a non-compatible liquid medium to polymerize the emulsion with a soluble cationic initiator, giving as a result a colloid of spherical polymeric nanoparticles. The polymerization has been carried out in a 50 mL three-neck round-bottom flask immersed in a water bath at 70°C by first stirring 1 mM $C_8H_{18}N_6$-2HCl + 2.26 M $C_5H_8O_2$ with nitrogen bubbling in deionized water. At the beginning of the polymerization reaction, the addition of a second solution consisting of 2 mM $C_5H_6O_4$ (itaconic acid) is needed to reduce the surface tension of the final PMMA colloidal suspension and to obtain porous membranes without cracks. Although the polymerization reaction lasts approximately 30 minutes, as identified by a gradual increase in the temperature of the suspension to 75°C, agitation and nitrogen bubbling is maintained for a further 7 hours. After this time, a suspension based on 150

nm diameter PMMA nanoparticles is obtained. Continuous colloidal membranes are then fabricated by the drop-casting method, in which 100 μL of PMMA colloidal suspension is dropped onto the glass/ITO substrates [41]. After water evaporation, self-assembly of PMMA spheres resulted in compact opal templates, which were annealed above the glass transition temperature ($T_g \approx 105°$C) of atactic PMMA for 30 minutes to fuse adjacent nanoparticles between each others. Composite Ni, Co, and Ni_xCo_{1-x} ($0 \leq x \leq 1$) 3D-IOs have been grown into the interstitial voids of the PMMA membranes by a standard three-probe electrodeposition technique at room temperature in the potentiostatic mode using a Ag/AgCl reference electrode and a Pt counter electrode. The growth of Co and Ni composite 3D-IOs has been carried out at the respective constant potentials of -0.95 V and -1.1 V by using the following electrolytic solutions: 238.5 [g l^{-1}] $CoSO_4 \cdot 7H_2O$ + 30 [g l^{-1}] H_3BO_3; and 262.8 [g l^{-1}] $NiSO_4$ + 30 [g l^{-1}] H_3BO_3 at pH 3.4. The pH value of the as-prepared Co electrolyte is 3.8, which has been increased up to 5.0 by the addition of NaOH [42]. For the electrodeposition of the Ni_xCo_{1-x} (20% $\leq x \leq$ 75%) alloyed inverse opals, a constant reduction potential in the range from -0.85 to -2 V and an electrolyte containing 26.3 [g l^{-1}] $NiSO_4 \cdot 6H_2O$ + 44.9 [g l^{-1}] $CoSO_4 \cdot 7H_2O$ + 30.3 [g l^{-1}] H_3BO_3 were used. Electrodeposition of alloyed inverse opals with 60% $\leq x \leq$ 90% was done for reduction potentials in the range from -1 to -2 V using the same electrolyte but with a Co concentration of 12.2 [g l^{-1}] $CoSO_4 \cdot 7H_2O$ instead. The pH of these solutions was lowered down to 2.0 by addition of H_2SO_4.

The inverse opals morphology has been confirmed by field-emission scanning electron microscopy (FE-SEM) observations after removal of the PMMA host membrane using dichloromethane. The crystal orientation has been investigated by X-ray diffraction (XRD) experiments using a Bruker D2 Phaser X-ray diffractometer with a Cu radiation source of wavelength $\lambda = 1.54$ Å. For the room temperature magneto-
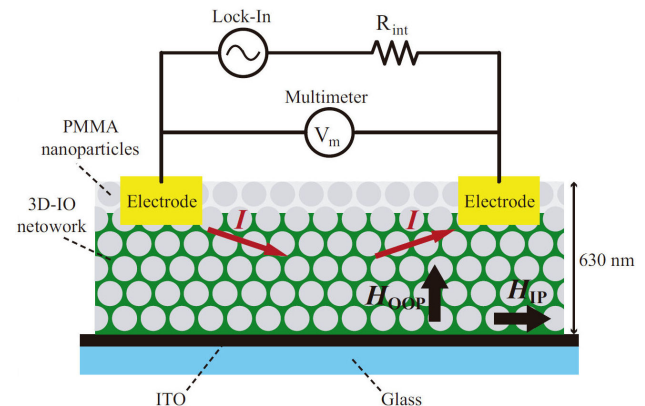

FIGURE 1. Schematic representation of the electrical circuit for magneto-transport measurements of a 3D-IO network grown on an ITO/glass substrate. A Lock-In amplifier and a digital multimeter are used to inject an AC electrical signal and to record the sample resistance R, respectively, while the applied magnetic field is sweep either along the IP or OOP direction to the film plane.
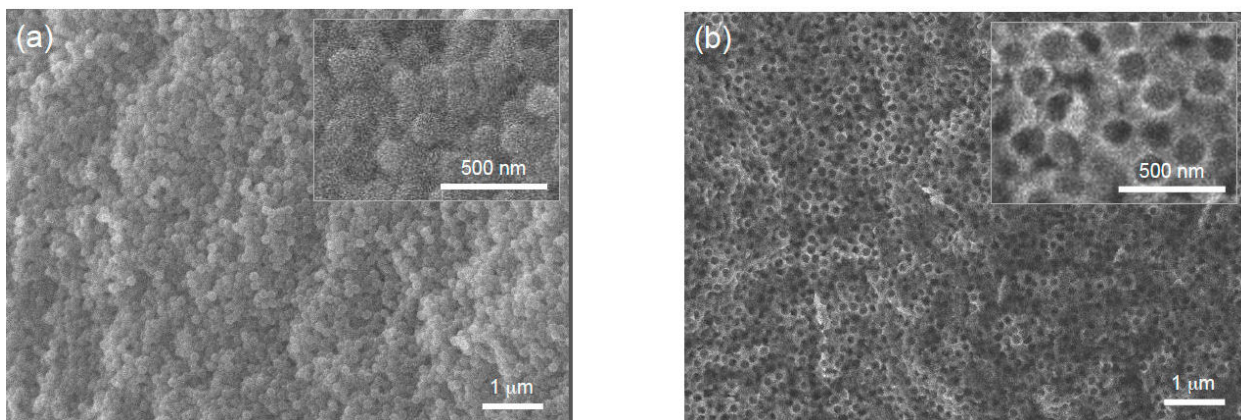
FIGURE 2. Scanning electron microscopy micrographs of a) the top view of a porous membrane made of self-assembled PMMA spherical nanoparticles, and b) the corresponding Ni 3D-IO synthesized by electrodeposition in the porous membrane shown in a). The inset in each figure shows a close view of the corresponding structure.

transport measurement setup a 7265 model lock-In amplifier has been used to inject an AC electrical current (I) in a two-probe setup while sweeping the magnetic field (H) between ± 10 kOe in the in-plane (IP) and out-of-plane (OOP) directions of the 3D-IO/polymer composite, as shown in the schematic view of Fig. 1. As seen, a digital multimeter is connected in parallel configuration to record the sample resistance. The two-layer ITO/3D-IO stacking allows the current to be injected directly into the branched 3D-IO structure because of its lower electrical resistance by three orders of magnitude in comparison to that of the ITO layer. The length between contacts made by an acetone-based Ag paint in the samples was about 0.5 cm. The input power to each sample was kept below 0.1 μW to avoid self-heating and to keep the resistance within its ohmic regime with a resolution of one part in 10^5.

3. Results and discussion

The as-obtained porous membranes consisting in disordered self-assembled PMMA spherical nanoparticles are shown in Fig. 2a). As seen, a distribution of voids in the membrane exists due to the high disordering of the PMMA particles. The inset in this figure shows a close view of the membrane top view, exhibiting spherical nanoparticles of almost the same diameter of about 150 nm. Figure 2b) shows the metallic 3D-IO obtained after dissolution of the host polymer membrane, which exhibits a dense interconnected morphology. The close view of the 3D-IO structure observed in the inset of this figure reveals the thickness of necks and walls in the range of 40 nm to 60 nm, which is very suitable for carrying out adequate magneto-transport experiments.

Besides, Fig. 3 displays XRD patterns for pure Co and Ni, as a well as for alloyed $Ni_{34}Co_{66}$, $Ni_{76}Co_{24}$ 3D-IOs. As seen, the diffraction pattern of the pure Co 3D-IO displays two main peaks at low 2θ angles, consistent with the Co hcp phase (COD 1512501). As the Ni content in the alloy increases to 34%, both the fcc and hcp phases of Co (COD
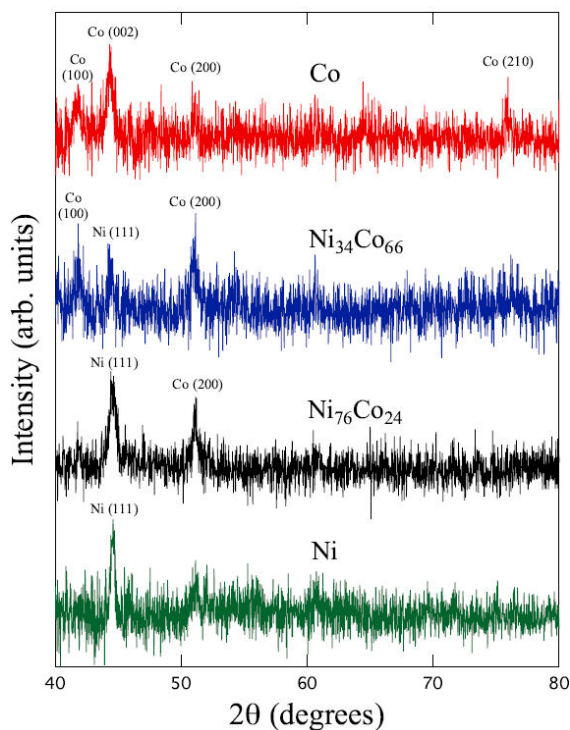

FIGURE 3. X-ray diffraction patterns for Co, $Ni_{34}Co_{66}$, $Ni_{76}Co_{24}$, and Ni 3D-IOs.

9008466) coexist with the fcc phase of Ni (COD 1512526). Although, the peak intensity for the fcc (200) plane is comparable to that for the hcp (100) plane, the XRD pattern is consistent with those for Co-rich alloys reported previously for thin films [43] and nanowires [44] grown by electrodeposition. Increasing further the Co content in the alloy to obtain the $Ni_{76}Co_{24}$ 3D-IO, leads to the disappearance of the Co (100) peak at the expense of the increase of the Ni (111) texture. In turn, the XRD pattern for the pure Ni 3D-IO network displays only the peak for the (111) plane.

On the other hand, the room temperature magnetoresistance curves shown in Fig. 4 are consistent with the depen-
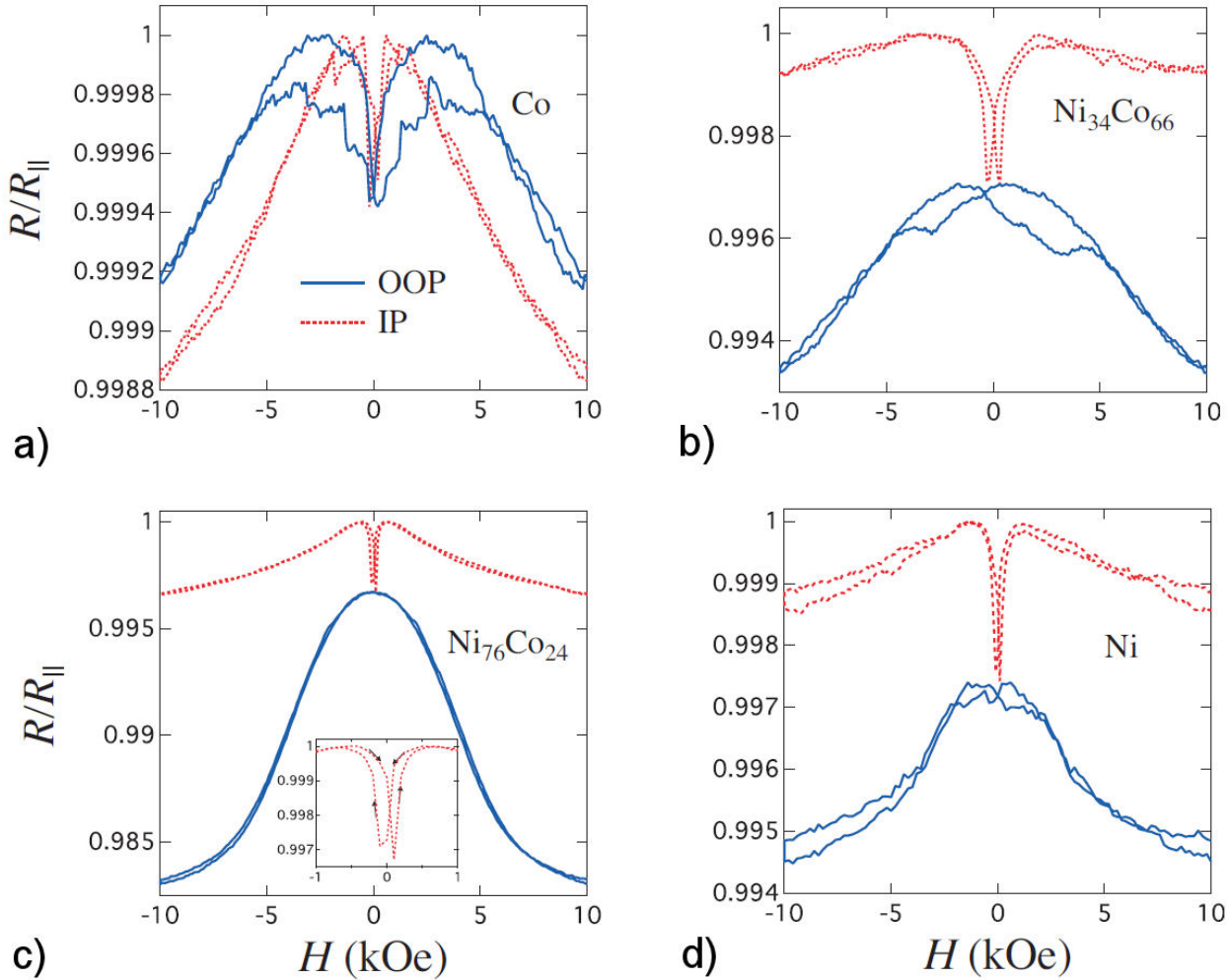
FIGURE 4. Room temperature magnetoresistance curves recorded with the magnetic field applied along the IP direction (dotted lines) and the OOP direction (continuous lines) for $Ni_x Co_{1-x}$ ($0 \leq x \leq 1$) 3D-IOs.

dence of resistivity with the relative angle between the magnetization and electrical current. This behavior is characteristic of the AMR effect, as corroborated by the different curves recorded with the external magnetic field applied in the OOP (continuous lines) and IP (dashed lines) directions of NiCo 3D-IOs. For the case of the pure Co 3D-IO, the IP and OOP curves shown in Fig. 4a) are very similar to each other, which is consistent with the presence of the magnetocrystalline (MC) anisotropy contribution that results from the predominant *hcp* phase (see Fig. 3). This anisotropy contribution has the effect of deviating the magnetization away from its preferential orientation along the necks and walls of the interconnected 3D-IO structure. This feature is confirmed by the significant decrease of the resistance near zero field along the OOP direction, as observed in Fig. 4a). In the absence of the MC anisotropy field, the magnetization tends to be aligned along the longest direction of the interconnection nanoelements in the 3D-IO structure. Indeed, the low dimensions in the 40 nm to 60 nm range of the interconnection necks and walls of the 3D-IO networks are close to the domain wall width of Ni-based ferromagnetic nanomate-

rials [44], favouring the local single domain regime and making 3D-IO ferromagnetic networks magnetically much harder in comparison to continuous thin films, as suggested by previous works [43, 44]. Furthermore, a residual MC anisotropy contribution in Co-rich 3D-IOs like that shown in Fig. 4b) is evident because of the magnetoresistance curves recorded along the OOP direction still display some hysteresis. That is, the reduction of the hysteresis in the OOP curve is consistent with the decrease of the *hcp* texture by virtue of the presence of Ni and Co *fcc* phases, as seen in Fig. 3.

Conversely, negligible hysteresis and the largest resistance difference between the IP and OOP resistance curves at saturation (± 10 kOe) is observed for the $Ni_{76}Co_{24}$ 3D-IO. For Ni-rich 3D-IOs the maximum resistance in the OOP direction is reached at zero field, as seen in Figs. 4c) and 4d). Therefore, for these networks the preferred alignment of the magnetization lies in the elongated necks and wall segments of the 3D structure because of to the predominance of the magnetostatic (MS) anisotropy. Indeed, in this case the 3D-IO microstructure is consistent with the polycrystalline cubic phase of Ni which has a negligible magnetocrystalline
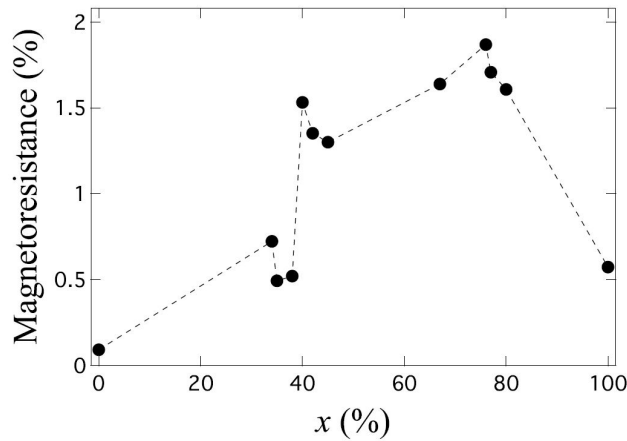
FIGURE 5. Variation of the room temperature MR ratio vs. the Ni content x for Ni_xCo_{1-x} 3D-IOs.

anisotropy [45]. Furthermore, whereas the OOP resistance curve is bell-shaped for most of the alloy compositions, the IP curve displays a complete different behavior as they have two minima in the vicinity of zero field which are attained after a sudden decrease of the resistance. These resistance minima are consistent with a very fast magnetization reversal dominated by vortex-like domain walls propagation.

The magneto-transport properties of the 3D-IOs synthesized in this work have been analyzed in terms of the conventional magnetoresistance (MR) ratio which is defined as the percentage change between the saturation (R_s) and maximum (R_m) resistance states, that is

$$\text{MR} = \frac{\Delta R}{R} = \frac{R_m - R_s}{R_s}. \tag{1}$$

As known, the physical mechanisms giving rise to this effect in ferromagnetic materials is originated by the spin-orbit coupling and the magnetic ordering, and corresponds mainly to the AMR ratio [46]. Figure 5 shows the room temperature MR ratio as a function of the Ni content (x) for Ni_xCo_{1-x} 3D-IOs. The observed behavior in this figure is consistent with what is reported in previous works on NiCo alloys and electrodeposited films [43,47], where the maximum MR ratio value of about 1.9% at $x \approx 75\%$ is attributed to the zero magnetostriction, zero MC constants and to the high saturation magnetization of about one Bohr magneton per atom for that particular alloy composition [46]. This MR value is smaller than previously reported AMR ratios for thin films and bulk alloys of up to $\approx 6\%$. In the case of 3D-IOs, the large disorder and number of interconnections between nanoscale necks and walls in the 3D-IO structure lead to a significant number of static lattice defects responsible of electron scattering responsible of a larger residual resistivity ρ_0. Despite this

drawback, the larger MR value close to 2% obtained in this work is large enough to be exploited in AMR based sensing applications like position sensors and flowmeters.

4. Conclusions

Self-assembled polymer opals have been used as templates for the synthesis by electrodeposition of disordered 3D-IOs made of pure ferromagnetic Ni and Co metals and their alloys. The structural characterization by X-ray diffraction has revealed the presence of mixed *fcc-hcp* phases in Co-rich 3D-IOs and a preferential *fcc* polycrystalline phase for Ni-rich 3D-IOs. The ability to perform reliable magneto-transport measurements has been demonstrated by virtue of the very high interconnectivity of the synthesized 3D-IOs. Particularly, the control of the NiCo 3D-IOs alloys composition has a great influence on the magnetoresistive response, leading to magnetoresistance ratios as high as 1.9% for the specific $Ni_{76}Co_{24}$ alloy. The present study opens up the way for a cost-effective porous template-assisted synthesis of interconnected 3D-IOs with accurate control over chemical composition, microstructural features and tunable magneto-transport properties. Despite the disordered feature of these networks, their magneto-transport properties make them suitable nanocomposite systems for the their potential application in magnetic field sensing and spintronic devices.

Acknowledgements

Declaration of Competing Interest

The authors declare that they have no known competing financial interests or personal relationships that could have appeared to influence the work reported in this paper.

CRediT authorship contribution statement

Hiram E. Torres Soto: Methodology, Validation, Data Curation. Flavio Abreu Araujo: Supervision, Writing - review & editing, Formal analysis, Validation Joaquín de la Torre Medina: Conceptualization, Supervision, Funding acquisition, Formal analysis, Writing - Original Draft.

1. L. Zhang *et al.*, Dynamic domain motion of thermalmagnetically formed marks on CoNi/Pt multilayers, *Journal of Applied Physics* **100** (2006) 053901.

2. G. Hrkac, J. Dean, and D. A. Allwood, Nanowire spintronics for storage class memories and logic, *Philosophical Transactions of the Royal Society of London A: Mathematical, Physical and Engineering Sciences* **369** (2011) 3214.

3. E. Spada *et al.*, Anisotropic magnetoresistance in electrodeposited cobalt antidot arrays, *Journal of Magnetism and Magnetic Materials* **320** (2008) e253, https://doi.org/10.1016/j.jmmm.2008.02.057.

4. M. Coïsson *et al.*, Anisotropic magneto-resistance in Ni80Fe20 antidot arrays with different lattice configurations, *Applied Surface Science* **316** (2014) 380, https://doi.org/10.1016/j.apsusc.2014.08.014.

5. S. H. Skjærvø *et al.*, Advances in artificial spin ice, *Nature Reviews Physics* **2** (2020) 13, https://doi.org/10.1038/s42254-019-0118-3.

6. A. Fernández-Pacheco *et al.*, Three-dimensional nanomagnetism, *Nat. Commun.* **8** (2017) 1, https://doi.org/10.1038/ncomms15756.

7. K. Gu *et al.*, Three-dimensional racetrack memory devices designed from freestanding magnetic heterostructures, *Nat. Nanotechnol.* **17** (2022) 1065, https://doi.org/10.1038/s41565-022-01213-1.

8. D. J. Shir *et al.*, Three-Dimensional Nanofabrication with Elastomeric Phase Masks, *The Journal of Physical Chemistry B* **111** (2007) 12945, https://doi.org/10.1021/jp074093j.

9. K. Shehzad *et al.*, Three-dimensional macro-structures of twodimensional nanomaterials, *Chem. Soc. Rev.* **45** (2016) 5541, https://doi.org/10.1039/C6CS00218H.

10. X. Wang, M. Ahmad, and H. Sun, Three-Dimensional ZnO Hierarchical Nanostructures: Solution Phase Synthesis and Applications, *Materials* **10** (2017), https://doi.org/10.3390/ma10111304.

11. P. Fischer *et al.*, Launching a new dimension with 3D magnetic nanostructures, *APL Materials* **8** (2020) 010701, https://doi.org/10.1063/1.5134474.

12. B. Luo and L. Zhi, Design and construction of three dimensional graphene-based composites for lithium ion battery applications, *Energy Environ. Sci.* **8** (2015) 456, https://doi.org/10.1039/C4EE02578D.

13. J. Grollier *et al.*, Neuromorphic spintronics, *Nature Electronics* **3** (2020) 360, https://doi.org/10.1038/s41928-019-0360-9.

14. T. da Câmara Santa Clara Gomes *et al.*, Magneto-Transport in Flexible 3D Networks Made of Interconnected Magnetic Nanowires and Nanotubes, *Nanomaterials* **21** (2021) 221, https://doi.org/10.3390/nano11010221.

15. E. C. Burks *et al.*, 3D Nanomagnetism in Low Density Interconnected Nanowire Networks, *Nano Letters* **21** (2021) 716, https://doi.org/10.1021/acs.nanolett.0c04366.

16. G. Guan *et al.*, Composition design and performance regulation of three-dimensional interconnected FeNi@carbon nanofibers as ultra-lightweight and high efficiency electromagnetic wave absorbers, *Carbon* **197** (2022) 494, https://doi.org/10.1016/j.carbon.2022.07.005.

17. A. A. Bykov *et al.*, Flux pinning mechanisms and a vortex phase diagram of tin-based inverse opals, *Supercond. Sci. Technol.* **32** (2019) 115004, https://doi.org/10.1088/1361-6668/ab3db7.

18. L. Wu e*t al.*, Hierarchically structured porous materials: synthesis strategies and applications in energy storage, *National Science Review* **7** (2020) 1667, https://doi.org/10.1093/nsr/nwaa183.

19. E. Armstrong *et al.*, Electrodeposited Structurally Stable V2O5 Inverse Opal Networks as High Performance Thin Film Lithium Batteries, *ACS Applied Materials & Interfaces* **7** (2015) 27006, https://doi.org/10.1021/acsami.5b09511.

20. Z. Liu *et al.*, Three-dimensional ordered porous electrode materials for electrochemical energy storage, *NPG Asia Materials* **11** (2019) 12, https://doi.org/10.1038/s41427-019-0112-3.

21. Y. zhen Liu *et al.*, Removal of gaseous pollutants by using 3DOM-based catalysts: A review, *Chemosphere* **262** (2021) 127886, https://doi.org/10.1016/j.chemosphere.2020.127886.

22. G. D. Mahan, N. Poilvert, and V. H. Crespi, Thermoelectric properties of inverse opals, *Journal of Applied Physics* **119** (2016) 075101, https://doi.org/10.1063/1.4941784.

23. L. Zhang, E. Reisner, and J. J. Baumberg, Al-doped ZnO inverse opal networks as efficient electron collectors in BiVO4 photoanodes for solar water oxidation, *Energy Environ. Sci.* **7** (2014) 1402, https://doi.org/10.1039/C3EE44031A.

24. J. Hou, M. Li, and Y. Song, Patterned Colloidal Photonic Crystals, *Angewandte Chemie International Edition* **57** (2018) 2544, https://doi.org/10.1002/anie.201704752.

25. M. Dabrowski *et al.*, Facile Fabrication of Surface-Imprinted Macroporous Films for Chemosensing of Human Chorionic Gonadotropin Hormone, *ACS Applied Materials & Interfaces* **11** (2019) 9265, https://doi.org/10.1021/acsami.8b17951.

26. Y.-J. Huang *et al.*, A facile approach to fabricate Ni inverse opals at controlled thickness, *Mater. Lett.* **63** (2009) 2393, https://doi.org/10.1016/j.matlet.2009.08.030.

27. S. O'Hanlon, D. McNulty, and C. O'Dwyer, The Influence of Colloidal Opal Template and Substrate Type on 3D Macroporous Single and Binary Vanadium Oxide Inverse Opal Electrodeposition, *J. Electrochem. Soc.* **164** (2017) D111, https://doi.org/10.1149/2.0121704jes.

28. E. Armstrong *et al.*, 3D Vanadium Oxide Inverse Opal Growth by Electrodeposition, *J. Electrochem. Soc.* **162** (2015) D605, https://doi.org/10.1149/2.0541514jes.

29. N. Sapoletova *et al.*, Controlled growth of metallic inverse opals by electrodeposition, *Phys. Chem. Chem. Phys.* **12** (2010) 15414, https://doi.org/10.1039/C0CP00812E.

30. C. Zhang *et al.*, In Situ Dual-Template Method of Synthesis of Inverse-Opal Co3O4@TiO₂ withWideband Microwave Absorption, *Inorg. Chem.* **60** (2021) 18455, `https://doi.org/10.1021/acs.inorgchem.1c03035`.

31. N. A. Grigoryeva, A. A. Mistonov, and S. V. Grigoriev, Small-Angle Neutron Diffraction for Studying Ferromagnetic Inverse Opal-Like Structures, *Crystallogr. Rep.* **67** (2022) 93, `https://doi.org/10.1134/S1063774522010060`.

32. D. Van Opdenbosch *et al.*, An Experiment-Based Numerical Treatment of Spin Wave Modes in Periodically Porous Materials, *Phys. Status Solidi B* **257** (2020) 1900296, `https://doi.org/10.1002/pssb.201900296`.

33. L. Wang *et al.*, Linear magnetoresistance in three-dimensional carbon nanostructure with periodic spherical voids, *Appl. Phys. Lett.* **107** (2015) 023103, `https://doi.org/10.1063/1.4926606`.

34. D. Apalkov, B. Dieny, and J. M. Slaughter, Magnetoresistive Random Access Memory, *Proc. IEEE* **104** (2016) 1796, `https://doi.org/10.1109/JPROC.2016.2590142`.

35. M. E. Kiziroglou *et al.*, Orientation and symmetry control of inverse sphere magnetic nanoarrays by guided self-assembly, *Journal of Applied Physics* **100** (2006) 113720, `https://doi.org/10.1063/1.2386936`.

36. T. da Câmara Santa Clara Gomes *et al.*, Magnetic and Magnetoresistive Properties of 3D Interconnected NiCo Nanowire Networks, *Nanoscale Res. Lett.* **11** (2016) 1, `https://doi.org/10.1186/s11671-016-1679-z`.

37. M. Akin *et al.*, Paper-Based Magneto-Resistive Sensor: Modeling, Fabrication, Characterization, and Application, *Sensors* **18** (2018) 4392, `https://doi.org/10.3390/s18124392`.

38. G. Williams *et al.*, Two-photon lithography for 3D magnetic nanostructure fabrication, Nano Res. **11** (2018) 845, `https://doi.org/10.1007/s12274-017-1694-0`.

39. S. J. Limmer, S. V. Cruz, and G. Z. Cao, Films and nanorods of transparent conducting oxide ITO by a citric acid sol route, *Applied Physics A* **79** (2004) 421, `https://doi.org/10.1007/s00339-004-2738-3`.

40. S. Gu *et al.*, Preparation of Micrometer-Sized Poly(methyl methacrylate) Particles with Amphoteric Initiator in Aqueous Media, *Langmuir* **20** (2004) 7948, `https://doi.org/10.1021/la049280c`.

41. S. H. Im *et al.*, Three-Dimensional Self-Assembly of Colloids at a Water-Air Interface: A Novel Technique for the Fabrication of Photonic Bandgap Crystals, *Advanced Materials* **14** (2002) 1367, `https://doi.org/10.1002/1521-4095(20021002)14:19⟨1367::AID-ADMA1367⟩3.0.CO;2-U`.

42. M. Darques *et al.*, Controlled changes in the microstructure and magnetic anisotropy in arrays of electrodeposited Co nanowires induced by the solution pH, *Journal of Physics D: Applied Physics* **37** (2004) 1411, `https://doi.org/10.1088/0022-3727/37/10/001`.

43. G. B. Tóth *et al.*, Temperature dependence of the electrical resistivity and the anisotropic magnetoresistance (AMR) of electrodeposited Ni-Co alloys, *The European Physical Journal B* **75** (2010) 167.

44. G. Ali and M. Maqbool, Fabrication of cobalt-nickel binary nanowires in a highly ordered alumina template via AC electrodeposition, *Nanoscale Research Letters* **8** (2013) 1.

45. B. D. Cullity and C. D. Graham, Introduction to Magnetic Materials, 2nd ed. (John Wiley & Sons, Inc., 2009).

46. T. McGuire and R. Potter, Anisotropic magnetoresistance in ferromagnetic 3d alloys, IEEE Transactions on Magnetics **11** (1975) 1018, 10.1109/TMAG.1975.1058782

47. N. V. Myung and K. Nobe, Electrodeposited Iron Group Thin-Film Alloys: Structure-Property Relationships, *Journal of The Electrochemical Society* **148** (2001) C136.